# AN INTEGRATED APPROACH TO THE ANALYSIS OF AMPLITUDE VARIATION WITH OFFSET IN VERTICAL TRANSVERSELY ISOTROPIC (VTI) MEDIA USING INCLUSION-BASED ROCK PHYSICS MODELING

HAMED GHANBARNEJAD-MOGHANLOO and MOHAMMAD ALI RIAHI

*Institute of Geophysics, University of Tehran, P.O. Box 14115-6466, Tehran, Iran.*
*hqanbarnejad@ut.ac.ir; mariahi@ut.ac.ir*

ABSTRACT

Ghanbarnejad-Moghanloo, H. and Riahi, M.A., 2023. An integrated approach to the analysis of amplitude variation with offset in Vertical Transversely Isotropic (VTI) media using inclusion-based rock physics modeling . *Journal of Seismic Exploration,* 32: 67-88.

For accurate lithology and fluid content characterization from the amplitude with offset analysis in hydrocarbon fields, understanding the shale anisotropy effect on reflectivity is essential. Shale-rich sedimentary deposits are common components of sedimentary sequences with strong anisotropic properties.  The main objective of this study is to perform anisotropic AVO analysis in vertical transversely isotropic (VTI) media at the top of a shale/gas sand interface, utilizing inclusion-based rock physics modeling in the Burgan formation in an Iranian oilfield. Results have shown that anisotropic AVO analysis shows Class I AVO which is indicative of the presence of hydrocarbon, whereas isotropic AVO analysis has shown no trend of any AVO classes. This study also investigates the application of a rock physics template in the shale\gas-sand interface in the Burgan formation. Without rock physics modeling, gas-sand can not be detected using the P- to S-wave velocity ratio against an acoustic impedance cross-plot. After rock physics modeling, gas sand has been discriminated from shale with a low P- to S-wave velocity ratio, low acoustic impedance, and high effective porosity in this cross-plot.

KEY WORDS: anisotropic AVO analysis, shale, inclusion-based rock physics, gas-sand, modeling, Vertical Transverse Isotropic (VTI) media, Burgan formation.

INTRODUCTION

Methods for amplitude variation with offset (AVO) analysis typically assume isotropic layers for the formations (Chopra and Castagna, 2014; Simm and Bacon, 2014). For almost isotropic mineral components, Zoeppritz equations and linearized approximations can be used to obtain a reasonable approximation for amplitude versus offset (AVO) response (Ghanbarnejad-Moghanloo and Riahi, 2022). Nevertheless, highly anisotropic minerals (such as interbedded shale) contribute to the uncertainty of amplitude versus offset (or angle) results. This assumption may have serious implications when the anisotropic parameters of different lithologies differ significantly (Ehirim and Chikezie, 2017; Asaka, 2018; Yan and Han, 2020). Anisotropy occurs when velocity varies with propagation direction, causing angular dependence of velocity and changing reflectivity with offset (Rüger, 2002; Chopra and Castagna, 2014; Asaka, 2018). In order to provide more reliable AVO analysis results, it is important to better understand the origin of anisotropy (Chopra and Castagna, 2014; Asaka, 2018;).

The effect of anisotropy on different aspects of seismic processing and interpretation has been investigated through various schemes. For instance, Bakulin (2003) described that Thomsen parameters (Thomsen, 1986) affect the elastic characteristics of VTI media. Tsvankin et al. (2010) discussed a brief overview of the modeling, processing, and inversion of seismic data for anisotropic media. Grechka et al. (2004) evaluated the shear wave presence in acoustic transverse media. Asaka (2018) has studied the effect of anisotropy in some seismic interpretation implications and demonstrated that it can significantly improve the results of prestack simulations and elastic impedance inversions in VTI media. Abedi et al. (2019) proposed a stretch-free NMO approach that automatically modifies input variables through anisotropic NMO correction.

Shale-rich sedimentary formations play a significant role in the propagation of elastic waves, primarily because of their anisotropic properties. The inorganic component of shale is formed by different minerals consisting of quartz, feldspar, pyrite, calcite, and dolomite as well as clay minerals such as chlorite, illite, kaolinite, and smectite. The layered structure of clay minerals causes elastic anisotropy (Vernik, 2016). Because anisotropic clay minerals align with the bedding plane, shales are often elastically anisotropic (Sayers and Dasgupta, 2019). Shale is generally considered to be transversely isotropic (TI) with a vertical axis of symmetry (Thomsen, 2012; Simm and Bacon, 2014; Wawrzyniak-Guz, 2019). In general, wave propagation parallel to layering is faster than wave propagation perpendicular to layering (Grechka 2009). In shale (which is, by definition, a fissile mudrock), the grains and intergranular pores generally lie parallel to bedding, and anisotropy can be significant (Johnston and Christensen, 1995; Vernik, 2016; Bala et al., 2019). Clay minerals are therefore highly anisotropic and have a platelet-like structure. (Simm and Bacon, 2014).

Hence, consideration of anisotropy could increase AVO analysis precision in shale intervals. The main objective of this paper is to study the anisotropy effect of the interface between shale and gas sand in amplitude variation with offset analysis using pre-stack seismic and well data in vertical transverse isotropy (VTI) media. Nevertheless, it is often difficult or impossible to obtain accurate logs of shale formations. Hence, it is necessary to apply rock physics modeling in petrophysical data to compensate for the shale effect in well-log data (Chopra and Castagna, 2014; Simm and Bacon, 2014).

For conventional shales, Vernik and Kachanov (2010) formulated an empirical relationship between bedding-normal P-wave velocity and porosity. Their shale model (SM), has been successfully applied by many authors (e.g., Vernik, 2016; Mur and Vernik, 2019; Sayers and Dasgupta, 2019; Wawrzyniak-Guz, 2019). In this study, the shale model is used to perform rock physics modeling in shale intervals.

Rock physics templates were primarily developed for siliciclastic rocks. Studies have been conducted on sands, sandstones, and shales to examine the relationship between lithology, fluid, and elastic properties. For instance, Avseth and Ødegaard (2004) developed the methodology of rock physics templates (RPT), a tool for estimating a reservoir's fluid and mineral composition by cross-plotting acoustic impedance against the P- to S-wave velocity ratio.

Ruiz and Cheng (2010) developed a rock physics model for tight gas sand based on a self-consistent (SC) model. Chi and Han (2009) studied unconsolidated sands from the Gulf of Mexico. A robust rock physics model for clay-rich source rocks is presented in Carcione and Avseth (2015). Prioul et al. (2004) developed a nonlinear rock physics model for estimating 3D subsurface stress in anisotropic formations. Several authors have successfully applied rock physics modeling in shale formations (e.g., Vernik and Milovac, 2011; Zhu et al., 2012; Guo et al., 2013; Dong et al., 2014; Khadeeva and Vernik, 2014; Wawrzyniak-Guz, 2019; Pan et al., 2020).

This study consists of four steps. As a first step, petrophysical information is modified by performing inclusion-based rock physic modeling to compensate for the effect of shale. In the second step, AVO attributes *A, B,* and *C* are extracted through analysis of amplitude versus offset. In the third step, Thomsen anisotropic parameters have been estimated using petrophysical data. Finally, using Thomsen parameters, an anisotropic AVO analysis has been performed on top of the Burgan formation in an Iranian oilfield. It has been shown that rock physics-based anisotropic AVO analysis has a great advantage over conventional isotropic AVO analysis in determining the top of a hydrocarbon reservoir. The synthetic models are used to test the efficacy of the described approach.

GEOLOGY AND AREA OF STUDY

The Zagros fold-thrust belt, which stretches more than 2000 km from southeastern Turkey to northern Syria and Iraq to western and southern Iran, containing numerous supergiant hydrocarbon fields, is the most productive fold-thrust belt worldwide (Alavi, 2004). During the Pliocene, the Zagros orogeny, part of the Alpine-Himalayan Mountain range, was folded and uplifted. The continental-continental collision folded the vast quantities of sediments that had been formed from Precambrian to Pliocene in the geosyncline in front of the Iranian plate as the Zagros mountains. (Kordi, 2019).

In the northern part of the Persian Gulf, most of the Cretaceous is characterized by the deposition of carbonate sediments over a northward dipping low ramp carbonate platform occasionally disrupted by massive clastic input from the southwest (e.g., Ratawi Shale, Zubair, Upper Shuaiba Member, Burgan, Nahr Umr Shale). These mixed carbonate-clastic shelfal systems extend over the whole Arabian Plate during the Early and Mid-Cretaceous and contribute to many of the giant oil fields in the region (Davies et al., 2002).

The Burgan Formation, Lower Cretaceous (Albian) sands, and shales are the lateral equivalent of the Kazhdumi formation in the Abadan Plain. This formation, and its equivalents (such as Nahr Umar Formation; Safaniya, and Khafji Members), form important reservoir rocks in several supergiants and many giant oil fields in the Middle East (Strohmenger et al., 2006; Van Buchem et al., 2010). This interval has substantially composed of loose to semi-consolidated Sands/Sandstones with interbedded shale on whole core samples (Fig. 1). In this study, rock physics-based anisotropic AVO analysis is investigated on top of this productive formation.
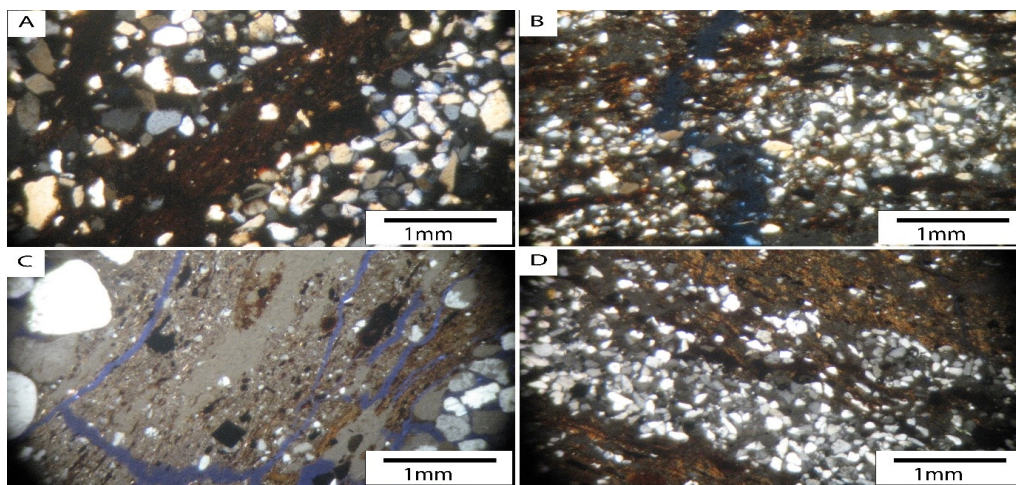


Fig. 1. Thin-section photomicrographs for Petrofacies: Flaser Sandstone (Sand with Silty Claystone); There is good connectivity in Flaser and Wavy structures (A: Depth: 2434.06 m; B: Depth: 2430.75 m; C: Depth: 2450.20 m; D: Depth: 2429.30 m) in Burgan formation.

The seismic data used in this study include a 3D pre-stack time migrated (PSTM) seismic CDP gathers with a time interval of 200 and 1000 ms in an approximate area of 11 km$^2$. Five wells were drilled in the study area, and fundamental petrophysical data, including sonic, shear wave velocity (in one well), RHOB, gamma-ray, and volume of clay for the extracting rock physics-based anisotropic AVO analysis workflow was available. Fig. 2 shows effective porosity, total porosity, and effective water saturation well logs for two wells as well as an arbitrary inline of seismic survey used in this study. Fig. 3 shows the workflow for extracting rock-physics-based anisotropic AVO analysis using joint use of pre-stack seismic and petrophysical data. In the first step, the quality of NMO-corrected Pre-stack gathers and well logs (sonic, DTSM, and clay content) has been assessed. In order to convert from offset to angle domain, a velocity model was built using Pre-stack seismic data and angle gathers have been reconstructed. The AVO attributes A, B and C have been extracted using generated angle gathers. The inclusion-based rock physics modeling has been built using well logs. Inclusion-based rock physics models have been constructed using well logs. Thomson parameters are then derived using modified sonic logs and clay volume. Based on Thomsen parameters, anisotropic P-P reflection amplitude at an angle of incidence $\theta$, $R_{app}(\theta)$ has been derived.
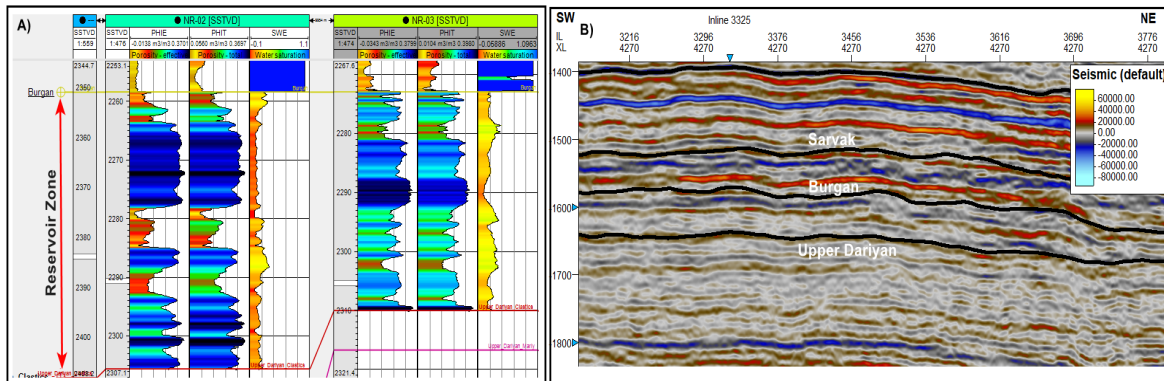


Fig. 2. A) Display of effective porosity, total porosity and effective water saturation for two wells in the study area and B) seismic profile used in this study. The reservoir zone is the Burgan to upper Dariyan interval.

ROCK PHYSICS MODELING

There are several rock physics relationships that define granular media as a random cluster of spherical grains. Spheres serve as ideal illustrations of grains in sandstone. Increased porosity leads to the loss of grain contact and reduced rigidity of porous materials, resulting in a reduction in stiffness (Mavko et al., 2020). Inclusion models provide an alternative method to granular media models in predicting elastic moduli of porous rocks. An inclusion model suggests that porous rocks are solid

matrixes containing inclusions (Kuster and Toksöz, 1974; Mavko et al., 2020). For a porous rock with a single type of inclusion, the dry-rock elastic moduli $K_{dry}$ and $\mu_{dry}$ are (Kuster and Toksöz, 1974; Grana et al., 2021):

$$K_{dry} = \frac{4K_{sol}\mu_{sol}(1-\varphi)}{3K_{sol}\varphi + 4\mu_{sol}} \quad , \tag{1}$$

$$\mu_{dry} = \frac{\mu_{sol}(9K_{sol}+8\mu_{sol})(1-\varphi)}{9K_{sol}+8\mu_{sol}+6(K_{sol}+2\mu_{sol})\varphi} \quad , \tag{2}$$

where $k_{sol}$ and $\mu_{sol}$ are the bulk modulus and the shear modulus of the solid phase, respectively and $\varphi$ is porosity.

Inclusion models approximate the rock as an elastic solid containing inclusion (i.e., pore). Xu-White (1995) describes a successful example of an inclusion model applied to well-log data. Pores in the Xu-White model are classified as clay-related and sand-related pores and each has its aspect ratio (the ratio between the longest and shortest axis). In general, clay particles generate pores with low aspect ratios, and crack-like pores will have limited stiffness, whereas sand grains will produce pores with larger, stiffer aspect ratios, and sub-spherical pores will have high stiffness (Simm and Bacon, 2014). Laboratory experiments found typical values of 0.02–0.05 for clay-related pores, 0.12 for sand-related pores, and 0.1 for carbonate-related pores (Simm and Bacon, 2014). In this study, we have used values of 0.035 and 0.12 for clay-related pores and sand-related pores, respectively.

The P-wave and S-wave velocities can be computed, by definition, from the bulk and shear moduli: $V_P = \sqrt{\frac{K+\frac{4}{3}\mu}{\rho}}$ and $V_S = \sqrt{\frac{\rho}{\mu}}$, where the density $\rho$ is generally computed as a linear average of the density of the solid and fluid phases, $\rho_{sol}$ and $\rho_{fl}$, weighted by porosity $\varphi$: $\rho = (1-\varphi)\rho_{sol} + \varphi\rho_{fl}$ (Grana et al., 2021).

In most rock physics models, homogeneous mineralogy is considered. Nonetheless, porous rocks generally consist of several mineral types (Grana et al., 2021). in these cases, mineral modules are averaged using elastic bounds based on volumetric fractions. Bounds were introduced in terms of the effective limits associated with porosity–velocity behavior, with the lower bound determined by the Reuss average (describing a suspension of minerals and fluids) and the upper bound by a modified Voigt bound. Narrower bounds are provided by the Hashin-Shtrikman (Hashin and Shtrikman, 1963) upper and lower bounds (Mavko et al., 2020).

To calculate P- and S-wave velocity using rock physics modeling in sand intervals (mostly quartz), eq. (1) and eq. (2) need to be solved. The bulk and shear modulus of the solid matrix for various minerals are given in

Table 1. Given porosity, dry-rock elastic moduli $K_{dry}$ and $\mu_{dry}$ could be calculated using eq. (1) and eq. (2). Therefore, rock physics-based P- and S-wave velocities are computed using dry bulk and shear modulus of the minerals and porosity of the layers of the zone of interest. In shaly intervals, Vernik and Kachanov (2010) were used. Finally, they are saturated using Gassmann's equation.
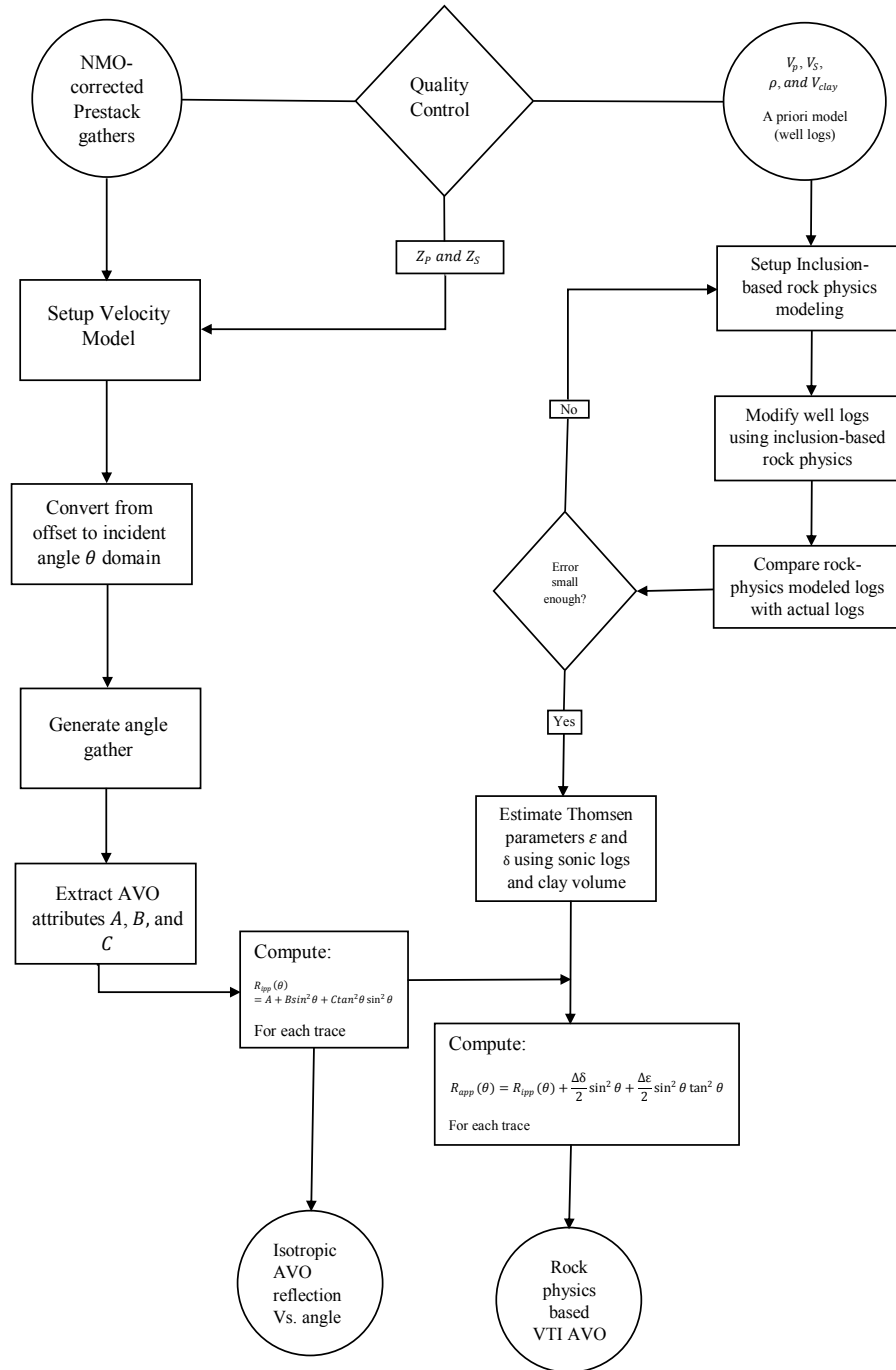


Fig. 3. The workflow illustrates the steps involved in extracting rock-physics-based anisotropic AVO analysis using joint use of pre-stack seismic and petrophysical data.

In most rock physics models, homogeneous mineralogy is considered. Nonetheless, porous rocks generally consist of several mineral types (Grana et al., 2021). in these cases, mineral modules are averaged using elastic bounds based on volumetric fractions. Bounds were introduced in terms of the effective limits associated with porosity-velocity behavior, with the lower bound determined by the Reuss average (describing a suspension of minerals and fluids) and the upper bound by a modified Voigt bound. Narrower bounds are provided by the Hashin-Shtrikman (Hashin and Shtrikman, 1963) upper and lower bounds (Mavko et al., 2020).

To calculate P- and S-wave velocity using rock physics modeling in sand intervals (mostly quartz), eq. (1) and eq. (2) need to be solved. The bulk and shear modulus of the solid matrix for various minerals are given in Table 1. Given porosity, dry-rock elastic moduli $K_{dry}$ and $\mu_{dry}$ could be calculated using eq. (1) and eq. (2). Therefore, rock physics-based P- and S-wave velocities are computed using dry bulk and shear modulus of the minerals and porosity of the layers of the zone of interest. In shaly intervals, Vernik and Kachanov (2010) were used. Finally, they are saturated using Gassmann's equation.

Table 1. Density, bulk modulus, and shear modulus of quartz, calcite, and sum of clays. *Sources of $k$, $\mu$, and $\rho$: 1 - Wawrzyniak-Guz (2019); 2 - Grana et al. (2021).*

| Mineral | $k$ (GPA) | $\mu$ (GPA) | $\rho$ ($\frac{gr}{cm^3}$) | Sources of $k$, $\mu$, and $\rho$ |
|---|---|---|---|---|
| Quartz | 36 | 45 | 2.65 | 2 |
| Calcite | 76 | 32 | 2.71 | 2 |
| Sum of clays | 39 | 25 | 2.70 | 1 |

Fig. 4 shows original and rock physics modeled petrophysical logs at a well location. Generally, P-wave velocity and density decrease at the top of the gas sand interface, while S-wave velocity increases slightly (Moghanloo et al., 2018; Simm and Bacon, 2014). Due to the presence of shale in this interval, the values for original logs of P-wave velocity, S-wave velocity, and density show no anomalous behavior atop the Burgan formation (Depth: 2418.58 m). Using rock physics modeling, the original petrophysical data are modified; therefore, P-wave velocity and density (Fig. 4a and Fig. 4c) decrease dramatically at the top of the Burgan formation which is a shale/gas sand interface (Depth: 2418 m), while S-wave velocity fairly decreases (Fig. 4b). These modified logs will be used in anisotropy estimation. Generally, the shale effect on petrophysics data has been corrected for the entire interval using rock physics modeling.

The relationship between fluid fill and rock properties is vital to the interpretation of seismic amplitudes (Simm and Bacon, 2014). Fluid substitutions at seismic frequencies are typically modeled using the Gassmann equation (Gassmann, 1951; Geertsma and Smit, 1961). To determine the bulk and shear moduli of dry rock at different saturations,

Gassmann's equation is applied. (Smith et al., 2003). it is worth mentioning that the shear modulus of saturated rock is equivalent to the shear modulus of dry rock. Gassmann's equations which computed the moduli $K_{sat}$ of saturated rock are as follows (Mavko et al., 2020):

$$K_{sat} = K_{dry} + \frac{\left(1 - \frac{K_{dry}}{K_{sol}}\right)^2}{\frac{\varphi}{K_{fl}} + \frac{1-\varphi}{K_{sol}} - \frac{K_{dry}}{K_{sol}^2}} \qquad , \tag{3a}$$

$$\mu_{sat} = \mu_{dry} \quad , \tag{3b}$$

where $K_{sat}$ and $\mu_{sat}$ are the bulk and the shear modulus of the saturated rock as a function of porosity and saturation, $K_{dry}$ and $\mu_{dry}$ are the bulk and the shear modulus of the dry rock frame, $K_{sol}$ is the bulk modulus of the skeleton (i.e., the effective bulk modulus of the multimineral matrix), and $K_{fl}$ is the bulk modulus of the fluid mixture (Table 2).
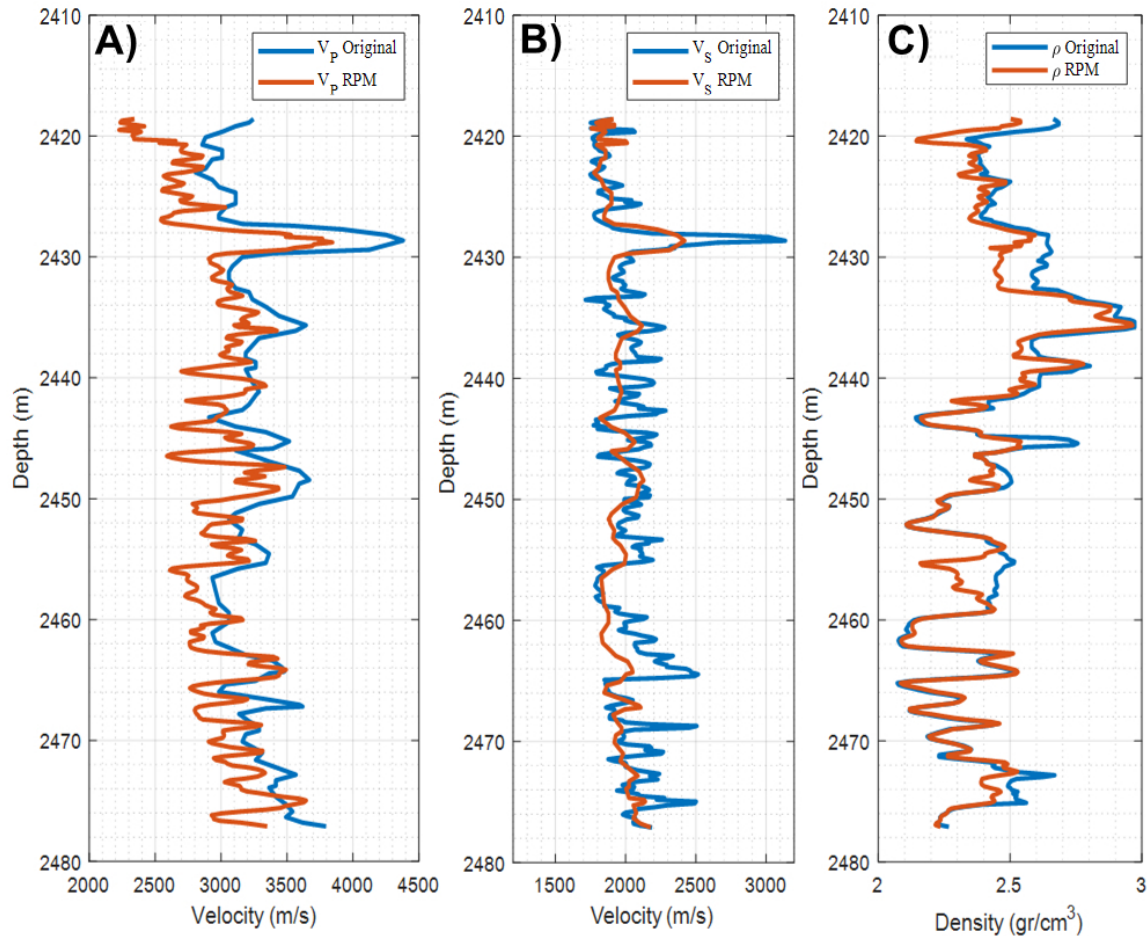


Fig. 4. Comparison between original and rock physics modeled petrophysical data. A) P-wave velocity, B) S-wave velocity and C) density. Rock physics modeling has been applied to petrophysical data to compensate for the shale effect in petrophysical data.

Table 2. Fluid properties used in rock physics modeling. *Sources* of $k$, $\mu$, and $\rho$:
1 - Wawrzyniak-Guz (2019);  2 - Grana et al. (2021).

| Fluid type | $k$ (GPA) | $\mu$ (GPA) | $\rho$ ($\frac{gr}{cm^3}$) | Sources of $k$, $\mu$, and $\rho$ |
|---|---|---|---|---|
| Water | 2.6 | 0 | 1.05 | 1 |
| Gas | 0.05 | 0 | 0.1 | 1 |
| Oil | 1 | 0 | 0.75 | 2 |

Finally, when the bulk and the shear moduli of saturated rock are calculated as a function of porosity and saturation, $K_{sat}(\varphi, S_w)$ and $\mu_{sat}(\varphi)$, one can compute $V_P$ and $V_S$ as follows Wawrzyniak-Guz (2019):

$$V_P(\varphi, S_w) = \sqrt{\frac{K_{sat}(\varphi,S_w)+\frac{4}{3}\mu_{sat}}{\rho_{sat}(\varphi,S_w)}} \quad , \tag{4a}$$

$$V_S(\varphi, S_w) = \sqrt{\frac{\mu_{sat}(\varphi)}{\rho_{sat}(\varphi,S_w)}} \quad , \tag{4b}$$

$$\rho_{sat}(\varphi, S_w) = \rho_{sol}(1 - \varphi) + \rho_w S_w \varphi + \rho_{hc}(1 - S_w)\varphi \quad , \tag{4c}$$

where $\rho_{sat}$, $\rho_{sol}$, $\rho_w$, $\rho_{hc}$ are the bulk density of saturated rock, the matrix, water, and hydrocarbon densities, respectively. As an example of the application of Gassmann's equations, the fluid substitution method is commonly used in rock physics studies to determine the saturated-rock elastic properties under different fluid conditions (Mavko et al., 2020).

The fluid substitution procedure has been applied to the petrophysical logs of the Burgan formation (Fig. 5). When pore fluid is gas, P-wave velocity, and density significantly decrease, whereas S-wave velocity increases slightly. The effect of oil on well-logs is less than that of gas, but it still reduces P-wave velocity, S-wave velocity, and density.

Rock physics modeling is used to develop more precise rock physics templates. The rock physics templates (RPT) were developed by Avseth and Ødegaard (2004), and it is very useful in determining the hydrocarbon signature, because of the low acoustic impedance and P-wave to S-wave velocity ratio in hydrocarbon formations (Moghanloo et al., 2018). Fig. 6A shows the P- to S-wave velocity ratio against acoustic impedance before rock physics moldering. As can be seen, gas sand could not be discriminated against using this cross plot before rock physics modeling. After rock physics modeling (Fig. 6B), gas-sand is discriminated in this cross plot with the highest effective porosity. Furthermore, a general trend is visible between acoustic impedance and P- to S-wave velocity ratio after performing rock physics modeling, as can be seen in Fig. 6B.
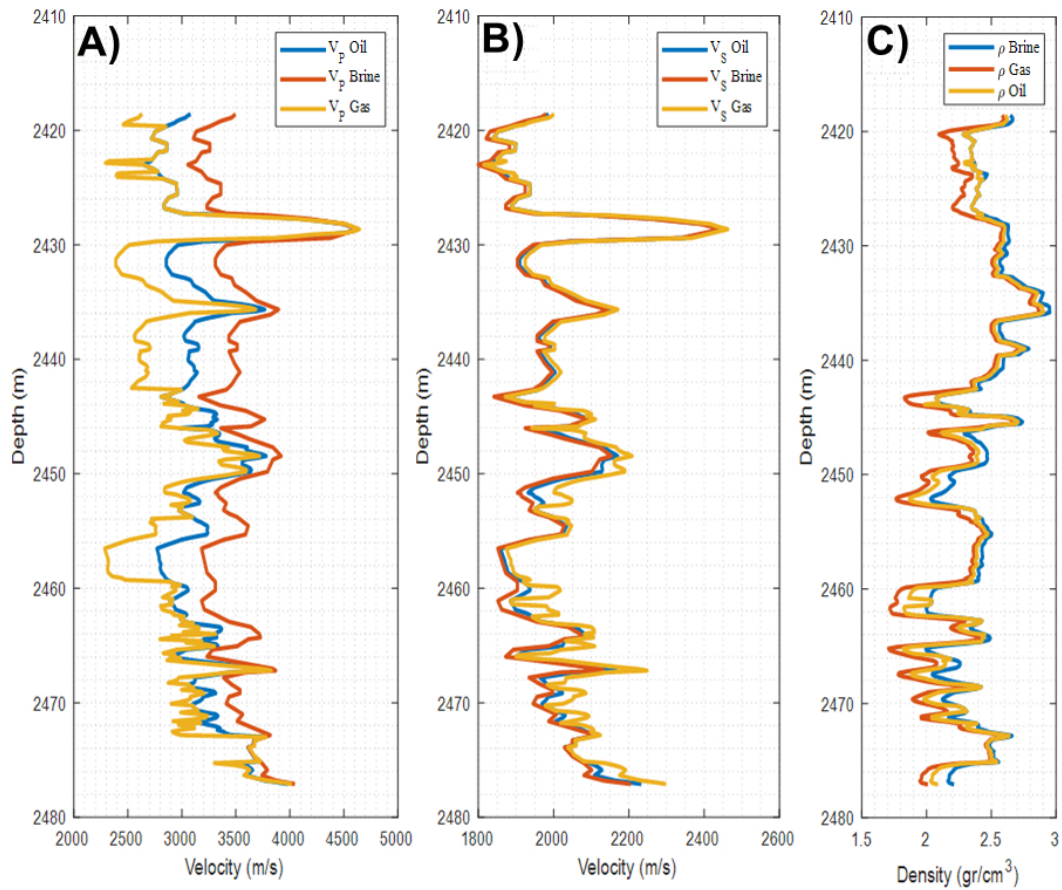
Fig. 5. Display of fluid substitution (water, oil, and gas) for A) P-wave velocity, B) S-wave velocity, and C) density.
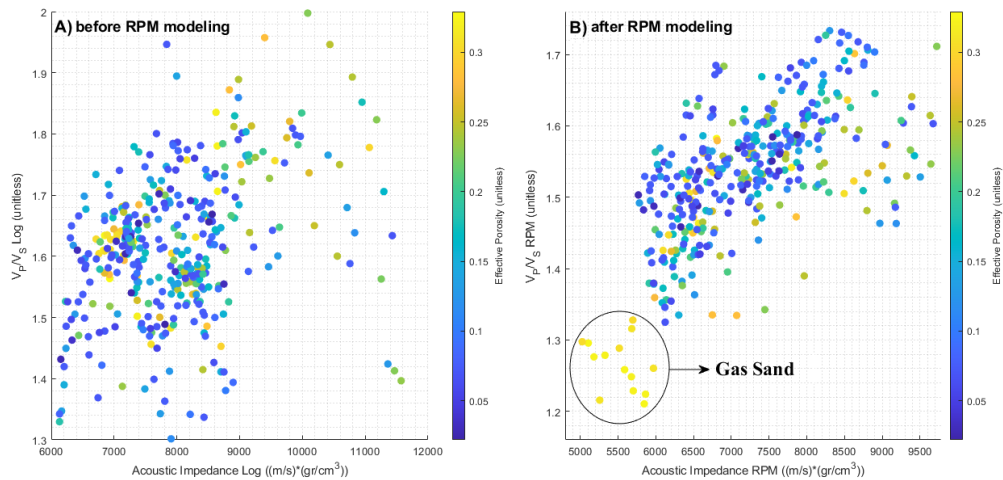


Fig. 6. Cross plot of $V_P/V_S$ vs. $AI$ A) before rock physics modeling and B) after rock physics modeling. The gas sand is discriminated with the highest effective porosity after rock physics modeling.

## RESULTS AND DISCUSSION

Before applying the integrated method in the Burgan formation, we have applied this approach to three synthetic models in shale/gas sand interfaces proposed by Kim et al. (1993) (Table 3) for different three AVO classes. Using given velocities, density, and clay volume (Table 3), Thomsen parameters were calculated using eq. (A-5) to eq. (A-7). Then, $\Delta\delta$ and $\Delta\varepsilon$ were calculated for each interval. Using derived Thomsen parameters, eq. (A-8) was solved which is reflection coefficient vs. angle of incidence in VTI media. Fig. 6 shows the isotropic and anisotropic reflection coefficient against the angle of incidence for the three models. As can be seen, the anisotropy influence on AVO analysis increases with increasing the angle of incidence. Therefore, the effect of anisotropy is more noticeable at larger offsets (or larger angles of incidence).

Table 3. Elastic and petrophysical parameters used in synthetic AVO analysis study in shale/gas sand interfaces.

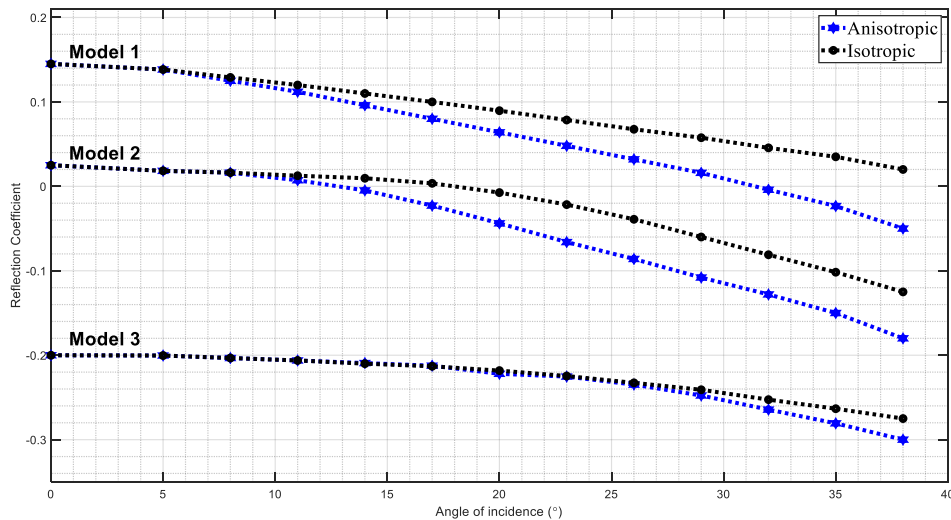| Parameters | Model 1 | | Model 2 | | Model 3 | |
|---|---|---|---|---|---|---|
| | Shale | Sand | Shale | Sand | Shale | Sand |
| $V_P \left(\frac{km}{s}\right)$ | 3.3 | 4.2 | 2.96 | 3.49 | 2.73 | 2.02 |
| $V_S \left(\frac{km}{s}\right)$ | 1.7 | 2.7 | 1.38 | 2.29 | 1.24 | 1.23 |
| $\rho \left(\frac{gr}{cm^3}\right)$ | 2.35 | 2.49 | 2.43 | 2.14 | 2.35 | 2.13 |
| $V_{Clay}$ | 0.89 | 0.00016 | 0.93 | 0.00013 | 0.96 | 0.00018 |



Fig. 7. Variation of elastic reflectivity with the angle of incidence for the three synthetic models of shale/gas sand reflectors in isotropic and VTI anisotropic media. The black and blue dashed curves are for isotropic and anisotropic material properties, respectively. The effect of anisotropy is more noticeable at a larger angle of incidents (or offsets).

Fig. 8 shows a section of intercept (A), gradient (B), and curvature (C) parameters in the reflection coefficient against the angle of incidence formula [eq. (8a)].
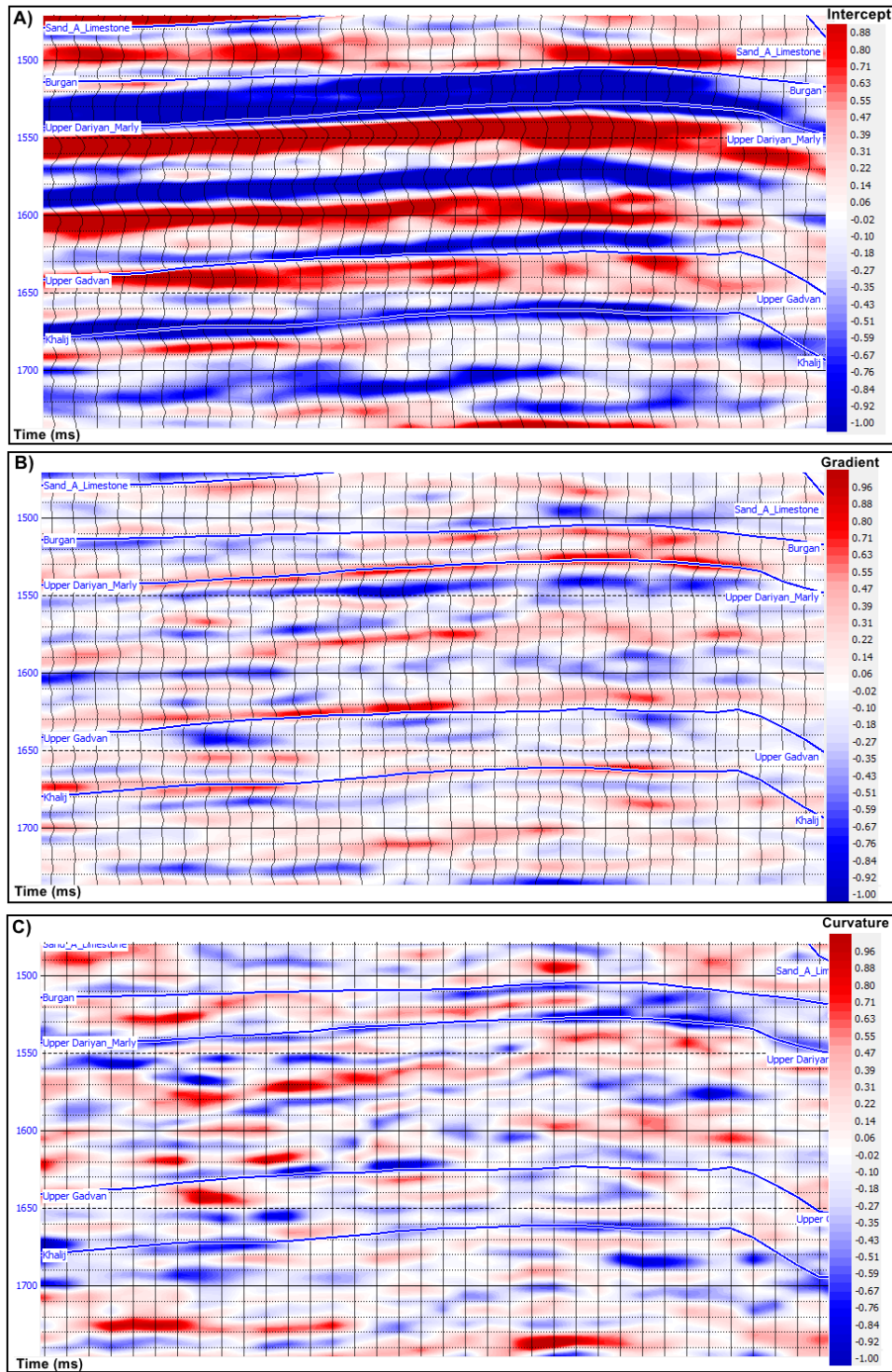


Fig. 8. The sections of Intercept (A), Gradient (B), and Curvature (C) parameters in an arbitrary inline.

Thomsen parameters were calculated using eq. (A-5) to eq. (A-7) in the Burgan formation at the well location (Fig. 9). At the top of the Burgan formation, clay volume and water saturation decrease, and therefore, Thomsen parameters ($\varepsilon$, $\gamma$, and $\sigma$) decrease. Generally, with increasing clay content (higher clay volume), anisotropic parameters increase. The reflection coefficient and statistical wavelet extracted from pre-stack seismic data as well as its power and phase spectrum are also shown in Fig. 9.
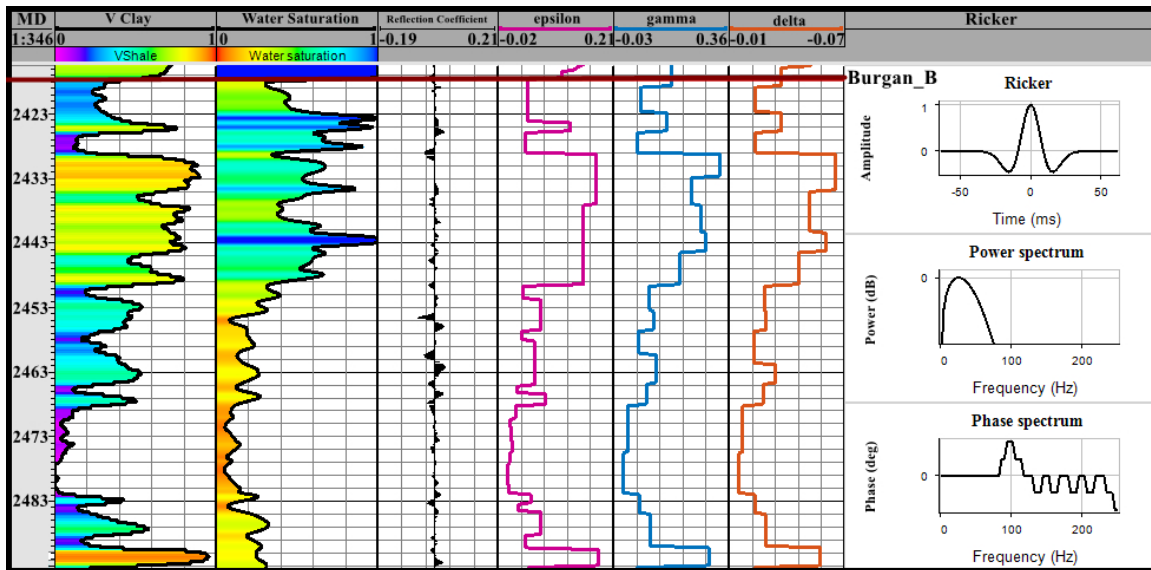


Fig. 9. From left to right: volume of clay, water saturation, reflection coefficient, Thomsen parameters at well location, and statistical wavelet extracted from pre-stack seismic data as well as its power and phase spectrum. An increase in clay content leads to increases in anisotropic parameters.

Fig. 10 shows cross plots of Thomsen parameters $\varepsilon$, $\gamma$, and $\sigma$. Color codes represent the clay volume for each sample. Samples with low clay volume (sand intervals) have less anisotropic properties, while samples with high clay volume (shale intervals) have more anisotropic properties. Therefore, with increasing clay content, Thomsen parameters increase.

Using given velocities, density, and clay volume (Table 3), Thomsen parameters were calculated using eq. (A-5) to eq. (A-7). Then, $\Delta\delta$ and $\Delta\varepsilon$ were calculated for each interval. Using derived Thomsen parameters, eq. (A-8) was solved which is the reflection coefficient vs. the angle of incidence in VTI media. Fig. 11 shows anisotropic amplitude variation versus angle of incidence. According to Fig. 11, in isotropic AVO analysis (red curve) there is no obvious AVO class. In other words, isotropic AVO analysis shows no presence of hydrocarbon on top of the Burgan formation. In anisotropic AVO analysis (blue curve), AVO class I is visible in the

reflection coefficient vs. the angle of incidence cross plot (Fig. 11) which is indicative of hydrocarbon on top of the Burgan formation.

Fig. 12 shows the pre-stack angle gather in isotropic and anisotropic media. In isotropic media, there is no visible AVO class. While in anisotropic media AVO class I (decreasing amplitude with increasing angle of the incident) is clear which indicates the presence of hydrocarbon.
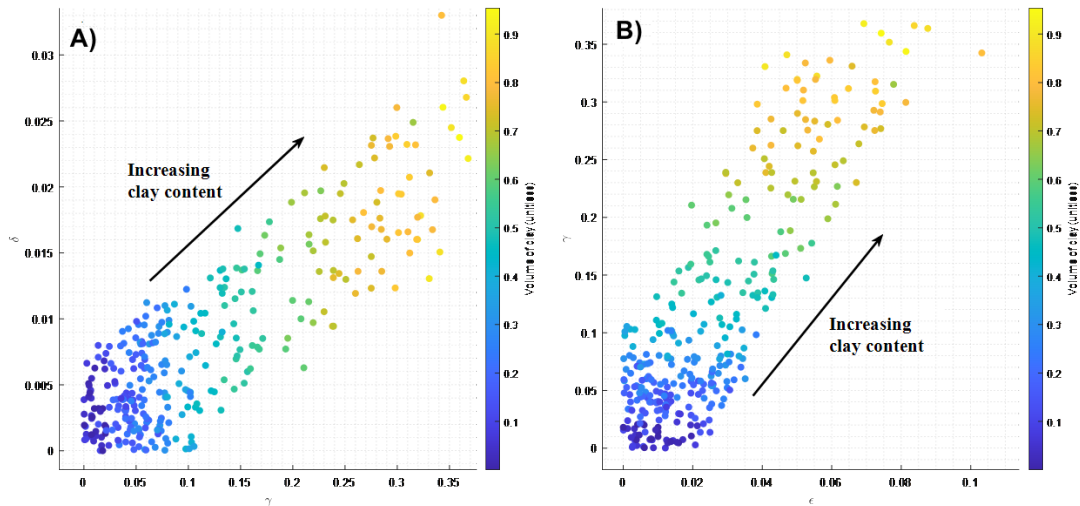


Fig. 10. Cross plots of Thomsen parameters: A) delta vs. gamma and B) gamma vs. epsilon. The sample's color represents the clay volume of each sample. Samples with low clay volume (sand intervals) have less anisotropic properties, while samples with high clay volume (shale intervals) have greater anisotropic properties.
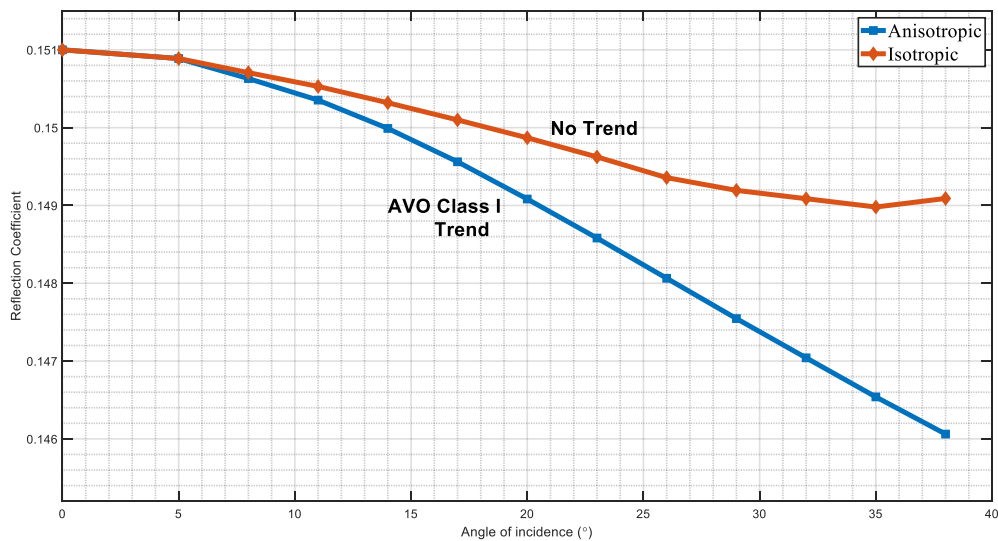


Fig. 11. Reflection coefficient versus angle of incidence in top of the Burgan formation in isotropic and anisotropic media. In isotropy media, there is no obvious trend. However, in anisotropic media, the cross plot shows AVO class I which represents the top of hydrocarbon.
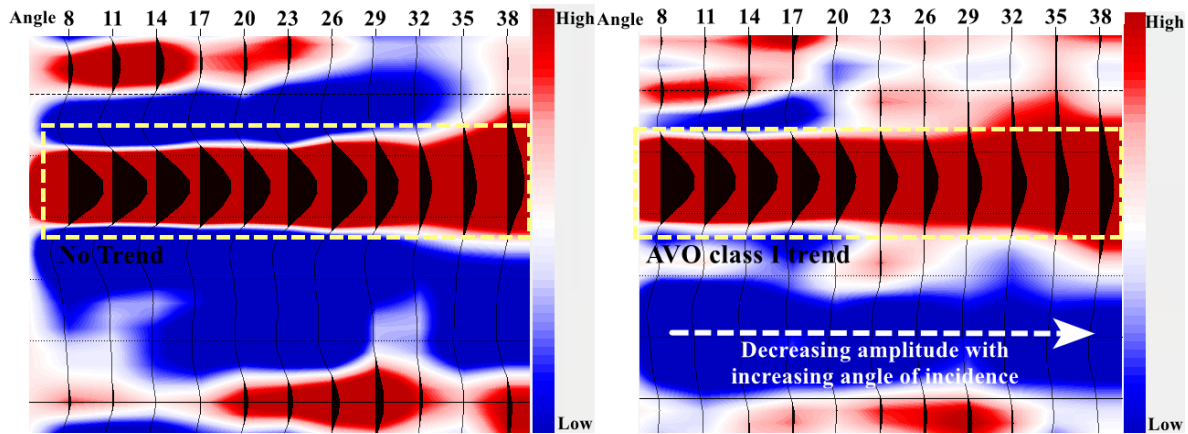
Fig. 12. Angle gathers in (left) isotropic and (right) anisotropic media in the shale/gas sand interface atop the Burgan formation. In isotropic media (left) there is no visible AVO class, while in anisotropic media (right) AVO class I is clear, indicating the presence of the hydrocarbon.

CONCLUSIONS

To obtain precise anisotropic AVO analysis, we use inclusion-based rock physics modeling on petrophysical data. We have used Kuster–Toksöz modeling for the sand interval. To do so, we solved eq. (1) and eq. (2) using bulk and shear modulus of minerals, provided in Table 1. Then, we obtained rock physics-based P- and S-wave velocity as well as density for sand intervals. Since clay minerals are strongly aligned in shale, the elastic properties of shale need to be modeled differently. Hence, the shale model (SM) has been used for shale intervals. We have shown that rock physics templates yield more accurate results after rock physics modeling. Hashin–Shtrikman bound was used to average the minerals modules based on the volumetric fractions for sand and shale intervals. The gas-sand is discriminated in acoustic impedance vs. P- to S-wave velocity ratio after rock physics modeling with acoustic impedance (< 6000 (m/s*g/cc)), P- to S-wave velocity ratio (<1.34), and high effective porosity. We have also used fluid substitution modeling to supervise the effect of different pore fluids on petrophysical data. Using petrophysical data (velocities, density, and clay volume), Thomsen parameters were estimated. Cross plots of Thomsen parameters (Fig. 10) show that, as expected, samples with low clay volume (sand intervals) have less anisotropic properties, while samples with high clay volume (shale intervals) have more anisotropic properties. We have shown that the effect of anisotropy is more noticeable at larger offsets (or larger angles of incidence) in both synthetic and real data. We show that using AVO analysis in VTI media, the AVO class I trend is clear, indicating the top of hydrocarbon in the Burgan formation, while in isotropic AVO no class is detected. Synthetic models have been generated to test the efficacy of the proposed workflow. The integrated approach helps to locate hydrocarbon zones more accurately, using anisotropic AVO analysis and utilizing inclusion-based rock physics modeling.

## ACKNOWLEDGMENTS

## REFERENCES

Abedi, M.M., Riahi, M.A. and Stovas, A., 2019. Three-parameter normal moveout correction in layered anisotropic media: A stretch-free approach. Geophysics, 84(3): C129-C142.

Alavi, M., 2004. Regional stratigraphy of the Zagros fold-thrust belt of Iran and its proforeland evolution. Am. J. Sci., 304: 1-20.

Asaka, M., 2018. Anisotropic AVO: Implications for reservoir characterization. The Leading Edge, 37: 916-923.

Avseth, P.A. and Ødegaard, E., 2004. Well log and seismic data analysis using rock physics templates. First break, 22(10): 37-43.

Bakulin, A., 2003. Intrinsic and layer-induced vertical transverse isotropy. Geophysics, 68: 1708-1713.

Bala, M., Cichy, A. and Wasilewska-Błaszczyk, M., 2019. Attempts to calculate the pseudo-anisotropy of elastic parameters of shales gas formations based on well logging data and their geostatistical analysis. Geol., Geophys., Environ., 45: 5-20.

Carcione, J.M. and Avseth, P., 2015. Rock-physics templates for clay-rich source rocks. Geophysics, 80(5): D481-D500.

Chi, X.G. and Han, D.H., 2009. Lithology and fluid differentiation using a rock physics template. The Leading Edge, 28: 60-65.

Chopra, S. and Castagna, J.P., 2014. Investigations in Geophysics - AVO. SEG, Tulsa, OK.

Davies, R.B., Casey, D.M., Horbury, A.D., Sharland, P.R. and Simmons, M.D., 2002. Early to mid-Cretaceous mixed carbonate-clastic shelfal systems: examples, issues and models from the Arabian Plate. GeoArabia, 7: 541-598.

Dong, N., Huo, Z.Z., Sun, Z.D., Liu, Z.S. and Sun, Y.Y., 2014. An investigation of a new rock physics model for shale. Chin. J. Geophys., 57: 1990-1998.

Ehirim, C.N. and Chikezie, N.O., 2017. The effect of anisotropy on amplitude versus offset (AVO) synthetic modeling in Derby field southeastern Niger Delta. J. Petrol. Explor. Product. Technol., 7: 667-672.

Gassmann, F., 1951. Über die Elastizität Poröser Medien. Vierteljahrsschrift der Naturforschenden Gesellschaft in Zürich, 96: 1-23.

Geertsma, J. and Smit, D.C., 1961. Some aspects of elastic wave propagation in fluid-saturated porous solids. Geophysics, 26: 169-181.

Ghanbarnejad-Moghanloo, H., and Riahi, M.A., 2022. Application of prestack Poisson dampening factor and Poisson impedance inversion in sand quality and lithofacies discrimination. Arab. J. Geosci., 15: 1-10.

Grana, D., Mukerji, T. and Doyen, P., 2021. Seismic Reservoir Modeling: Theory, Examples, and Algorithms. John Wiley & Sons, New York.

Grechka, V.I., 2009. Applications of Seismic Anisotropy in the Oil and Gas Industry. EAGE, Houten, Netherlands.

Grechka, V., Zhang, L. and Rector III, J.W., 2004. Shear waves in acoustic anisotropic media. Geophysics, 69: 576-582.

Guo, Z., Li, X.Y., Liu, C., Feng, X. and Shen, Y., 2013. A shale rock physics model for analysis of brittleness index, mineralogy, and porosity in the Barnett Shale. J. Geophys. Engineer., 10(2): 025006.

Hashin, Z. and Shtrikman, S., 1963. A variational approach to the elastic behavior of multiphase materials. J. Mechan. Phys. Solids, 11: 127-140.

Johnston, J.E. and Christensen, N.I., 1995. Seismic anisotropy of shales. J. Geophys. Res.: Solid Earth, 100(B4): 5991-6003.

Khadeeva, Y. and Vernik, L., 2014. Rock-physics model for unconventional shales. The Leading Edge, 33: 318-322.

Kim, K.Y., Wrolstad, K.H. and Aminzadeh, F., 1993. Effects of transverse isotropy on P-wave AVO for gas sands. Geophysics, 58: 883-888.

Kordi, M., 2019. Sedimentary basin analysis of the Neo-Tethys and its hydrocarbon systems in the Southern Zagros fold-thrust belt and foreland basin. Earth-Sci. Rev., 191: 1-11.

Kuster, G.T. and Toksöz, M.N., 1974. Velocity and attenuation of seismic waves in two-phase media: Part I. Theoretical formulations. Geophysics, 39: 587-606.

Li, Y., 2006. An empirical method for estimation of anisotropic parameters in clastic rocks. The Leading Edge, 25: 706-711.

Mavko, G., Mukerji, T. and Dvorkin, J., 2020. The Rock Physics Handbook. Cambridge University Press, Cambridge.

Moghanloo, H.G., Riahi, M.A. and Bagheri, M., 2018. Application of simultaneous prestack inversion in reservoir facies identification. J. Geophys. Engineer., 15: 1376-1388.

Mur, A. and Vernik, L., 2019. Testing popular rock-physics models. The Leading Edge, 38: 350-357.

Nye, J.F., 1985. Physical Properties of Crystals: Their Representation by Tensors and Matrices. Oxford University Press, Oxford.

Pan, X.P., Zhang, G.Z. and Chen, J.J., 2020.. The construction of shale rock physics model and brittleness prediction for high-porosity shale gas-bearing reservoir. Petrol. Sci., 17: 658-670.

Prioul, R., Bakulin, A. and Bakulin, V., 2004. Nonlinear rock physics model for estimation of 3D subsurface stress in anisotropic formations: Theory and laboratory verification. Geophysics, 69: 415-425.

Rüger, A., 2002. Reflection coefficients and azimuthal AVO analysis in anisotropic media. Expanded Abstr., 72nd Ann. Internat. SEG Mtg., Salt Lake City.

Ruiz, F. and Cheng, A., 2010. A rock physics model for tight gas sand. The Leading Edge, 29: 1484-1489.

Sayers, C.M. and Dasgupta, S., 2019. A predictive anisotropic rock-physics model for estimating elastic rock properties of unconventional shale reservoirs. The Leading Edge, 38: 358-365.

Simm, R. and Bacon, M., 2014. Seismic Amplitude: An Interpreter's Handbook. Cambridge University Press, Cambridge.

Smith, T.M., Sondergeld, C.H. and Rai, C.S., 2003. Gassmann fluid substitutions: A tutorial. Geophysics, 68: 430-440.

Strohmenger, C.J., Mitchell, J.C., Feldman, H.R., Lehmann, P.J., Broomhall, R.W., Patterson, P.E. and Al-Ajmi, N., 2006. Sequence stratigraphy and reservoir architecture of the Burgan and Mauddud formations (Lower Cretaceous), Kuwait. In: Harris, P.M. and Weber, L.J., Eds., Giant Hydrocarbon Reservoirs of the World: From Rocks to Reservoir Characterization and Modeling, AAPG Memoir 88/SEPM Special Publication, 213-245.

Thomsen, L., 1986. Weak elastic anisotropy. Geophysics, 51: 1954-1966.

Thomsen, L., 2012. On the use of isotropic parameters $\lambda$, E, $\nu$ to understand anisotropic shale behavior. Istanbul Internat. Geophys. Conf. (pp. 1-4). SEG - Chamber of Geophys. Engineers Turkey.

Tsvankin, I., Gaiser, J., Grechka, V., Van Der Baan, M. and Thomsen, L., 2010. Seismic anisotropy in exploration and reservoir characterization: An overview. Geophysics, 75(5): A15-A29.

Van Buchem, F.S., Baghbani, D., Bulot, L.G., Caron, M., Gaumet, F., Hosseini, A. and Vincent, B., 2010. Barremian-Lower Albian sequence stratigraphy of southwest Iran (Gadvan, Darivan, and Kazhdumi formations) and its comparison with Oman, Qatar, and United Arab Emirates. GeoArabia Special Publicat. 4: 503-548.

Vernik, L., 2016. Seismic Petrophysics in Quantitative Interpretation. SEG, Tulsa, OK.

Vernik, L. and Kachanov, M., 2010. Modeling elastic properties of siliciclastic rocks. Geophysics, 75(6): E171-E182.

Vernik, L. and Milovac, J., 2011. Rock physics of organic shales. The Leading Edge, 30: 318-323.

Wawrzyniak-Guz, K., 2019. Rock physics modeling for determination of effective elastic properties of the lower Paleozoic shale formation, North Poland. Acta Geophys., 67: 1967-1989.

Xu, S. and Payne, M.A., 2009. Modeling elastic properties in carbonate rocks. The Leading Edge, 28: 66-74.

Xu, S. and White, R.E., 1995. A new velocity model for clay-sand mixtures. 1. Geophys. Prosp., 43: 91-118.

Yan, F. and Han, D.H., 2020. Effect of seismic anisotropy on AVO interpretation: A Monte Carlo simulation study. Expanded Abstr., 90th Ann. Internat. SEG Mtg., Houston: 280-284.

Zhu, Y., Xu, S., Payne, M., Martinez, A., Liu, E., Harris, C. and Bandyopadhyay, K., 2012. Improved rock-physics model for shale gas reservoirs. Expanded Abstr., 82nd Ann. Internat. SEG Mtg., Las Vegas: 1-5.

## APPENDIX

## VERTICAL TRANSVERSE ISOTROPY (VTI) MEDIA

Subsurface rocks are composed of sets of cracks or layers. There are many rock types with homogeneous features along seismic wavelengths. Vertical transverse isotropy (VTI) describes the transverse isotropy of horizontally layered sedimentary rocks. (Chopra and Castagna, 2014; Simm and Bacon, 2014). Transversely isotropic systems are comprised of sequential thin layers or mineral grains aligned in thin layers (Chopra and Castagna, 2014; Wawrzyniak-Guz, 2019).

Fig. A-1A shows a model with VTI anisotropy. It assumes that all planes perpendicular to the axis of rotation have the same physical properties Fig. A-1B, is a Photomicrograph of organic-rich sandy/silty shale/marl layering in the Burgan formation. As can be seen, the fissility and parallel layering of shale intervals are visible on the slabbed core photo. Hence, it shows that shale formations in the Burgan formation could be described in a transversely isotropic model with a vertical axis of symmetry.
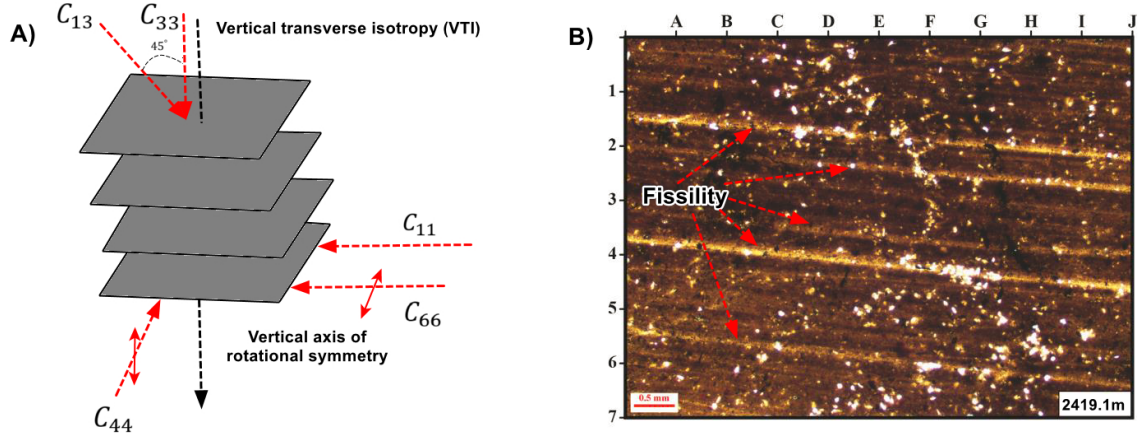
Fig. A-1. A) A model with VTI anisotropy; here, the layering determines the anisotropy and has a vertical axis of rotational symmetry, and B) Photomicrograph of organic-rich sandy/silty Shale/Marl layering in Burgan formation. Lamination and fissility are major features of the slabbed core photo. The Layering of Silt-sized quartz grains and organic matters are visible in photomicrographs in the zone of interest.

A TI medium has a hexagonal symmetry with five independents elastic stiffnesses (Mavko et al., 2020). Assuming the $x_3 -$ axis lies along the axis of rotational symmetry, the non-vanishing elastic stiffness coefficients are $C_{11} = C_{22},, C_{12} = C_{21}, C_{13} = C_{31} = C_{23} = C_{32}, C_{44} = C_{55}$. and $C_{66} = (C_{11} - C_{12})/2$ in the conventional two-index notation (Nye, 1985). The elastic stiffness matrix in Voigt notation can be written as:

$$C_{ij} = \begin{bmatrix} C_{11} & C_{12} & C_{13} & 0 & 0 & 0 \\ C_{12} & C_{11} & C_{13} & 0 & 0 & 0 \\ C_{13} & C_{13} & C_{33} & 0 & 0 & 0 \\ 0 & 0 & 0 & C_{44} & 0 & 0 \\ 0 & 0 & 0 & 0 & C_{44} & 0 \\ 0 & 0 & 0 & 0 & 0 & C_{66} \end{bmatrix} , \quad (A-1)$$

determines the horizontal compressional velocity ($C_{11} = \rho V_{P90}^2$), $C_{33}$ is the $M$ modulus which determines the vertical compressional velocity ($C_{33} = \rho V_{P0}^2$), $C_{44}$ is the $\mu$ modulus which controls the vertically traveling shear wave perpendicular to the layering and also the horizontally traveling shear wave with displacement perpendicular to the layering ($C_{44} = \rho V_{S0}^2$), $C_{66}$ controls the horizontally traveling shear wave with displacement parallel to the layering ($C_{66} = \rho V_{S9090}^2$) and $C_{13}$ controls propagation at oblique directions for both P- and S-waves ($C_{13} = -C_{44} + [4\rho^2 V_{P45}^2 (C_{11} + C_{33} + 2C_{44}) + (C_{11} + C_{44})(C_{33} + C_{44})]^{0.5}$). (Simm and Bacon, 2014; Wawrzyniak-Guz, 2019). Thomsen (1986) introduced three anisotropy parameters $\varepsilon$, $\gamma$, and $\sigma$ that have become conventional and common in geophysical applications:

$$\varepsilon = \frac{C_{11}-C_{33}}{2C_{33}} \quad , \tag{A-2}$$

$$\gamma = \frac{C_{66}-C_{44}}{2C_{44}} \quad , \tag{A-3}$$

$$\sigma = \frac{(C_{13}+C_{44})^2-(C_{33}-C_{44})^2}{2C_{33}\ (C_{33}-C_{44})} \quad . \tag{A-4}$$

Sonic logs measure only vertical velocities $V_{P0}$ and $V_{S0}$. Assuming horizontal bedding of geological formation and vertical wells, they are bedding-normal velocities. However, to solve eq. (A-2) to eq. (A-4), the horizontally traveling wave velocities are required. Therefore, acoustic logs cannot determine Thomsen parameters (Wawrzyniak-Guz, 2019). Nevertheless, Li (2006) proposed a method for computing $\varepsilon$, $\gamma$, and $\sigma$ directly from sonic logs and clay volume $V_{clay}$ as follows:

$$\varepsilon = \frac{\varepsilon_{clay}\cdot V_{clay}\cdot (V_{P0}-V_{P\ water})}{V_{P\ quartz}-V_{P\ water}-(V_{P\ quartz}-V_{P\ clay})\cdot V_{clay}} \quad , \tag{A-5}$$

$$\gamma = \frac{\gamma_{clay}\cdot V_{clay}\cdot V_{S0}}{V_{S\ quartz}-(V_{S\ quartz}-V_{S\ clay})\cdot V_{clay}} \quad , \tag{A-6}$$

$$\sigma = 0.32\varepsilon \quad , \tag{A-7}$$

where $\varepsilon_{clay}$, $\gamma_{clay}$ - Thomsen parameters of clay mineral, $V_{clay}$ - clay volume, $V_{P0}$, $V_{S0}$ - bedding-normal $P$- and $S$-wave velocities, $V_{P\ water}$ - an approximation of $P$-wave velocity, $V_{S\ quartz}$ - $P$- and $S$-wave velocities of quartz, $V_{P\ clay}$, $V_{S\ clay}$ - $P$- and $S$-wave velocities of clay. From laboratory data, Li (2006) derives the anisotropic parameters for clay minerals and proposes values: $\varepsilon_{clay}$= 0.6 and $\gamma_{clay}$ = 0.67. The other constants used in eq. (7a) and eq. (7b) are: $V_{P\ water}$= 1.5 km/s, $V_{P\ quartz}$ = 6.05 km/s, $V_{S\ quartz}$= 4.09 km/s (Li, 2006).

The angular dependence of velocity would influence reflectivity changes with offset due to anisotropy. For vertical transverse isotropy (VTI) media, P-P reflection amplitude at an angle of incidence $\theta$, $R_{app}(\theta)$, is calculated as follows (Chopra and Castagna, 2014):

$$R_{app}(\theta) = A + Bsin^2\theta + Ctan^2\theta \sin^2\theta + \frac{\Delta\delta}{2}\sin^2\theta + \frac{\Delta\varepsilon}{2}\sin^2\theta \tan^2\theta , \tag{A-8}$$

where:

$$A = \frac{1}{2}\left(\frac{\Delta V_P}{V_P} + \frac{\Delta \rho}{\rho}\right) \quad , \tag{A-9}$$

$$B = \frac{\Delta V_P}{2V_P} - 4\left(\frac{V_S}{V_P}\right)^2 \left(\frac{\Delta V_S}{V_S}\right) - 2\left(\frac{V_S}{V_P}\right)^2 \left(\frac{\Delta \rho}{\rho}\right) \quad , \tag{A-10}$$

$$C = \frac{1}{2}\frac{\Delta V_P}{V_P} \quad , \tag{A-11}$$

where

$$V_P = \frac{V_{p1}+V_{p2}}{2}, \; V_S = \frac{V_{S1}+V_{S2}}{2}, \; \rho = \frac{\rho_1+\rho_2}{2}, \; \left(\frac{V_S}{V_P}\right)^2 = \frac{\left(\frac{V_{S1}}{V_{P1}}\right)^2+\left(\frac{V_{S2}}{V_{P2}}\right)^2}{2},$$

$$\Delta V_P = V_{P2} - V_{P1},$$

$$\Delta V_S = V_{S2} - V_{S1}, \Delta \rho = \rho_2 - \rho_1, \Delta \varepsilon = \varepsilon_2 - \varepsilon_1 \text{ , and } \Delta \delta = \delta_2 - \delta_1.$$

Subscript 2 denotes the bottom layer and subscript 1 denotes the top layer.

The first three terms of eq. (8a) are isotropic reflectivity P-P reflection amplitude at an angle of incidence $\theta$ in isotropic media ($R_{inn}(\theta)$). The first term $A$ (intercept) in eq. (8a) is the zero-angle reflection coefficient related to the contrast of acoustic impedance, while the term $B$ (gradient) introduces the effect of shear velocity at non-zero angles. The term C (curvature) indicates the curvature of the amplitude response close to the critical angle. The first-order control on the intercept ($A$) is the acoustic impedance contrast. On the other hand, the sign and magnitude of the AVO gradient ($B$) is determined principally by the contrast of shear velocity across the interface (Simm and Bacon, 2014).